2020 IEEE/RSJ International Conference on Intelligent Robots and Systems (IROS)
October 25-29, 2020, Las Vegas, NV, USA (Virtual)

Development of Deployable Bending Wrist for Minimally Invasive Laparoscopic Endoscope

Jongwoo Kim[1], *Member, IEEE,* Thomas Looi[1], *Member, IEEE,* Allen Newman[2], James Drake[1], *Member, IEEE*

***Abstract*— During the last two decades, minimally invasive surgery (MIS) has become popular because it offers advantages such as less pain, faster recovery, improved cosmesis, and reduced complications. Single-port laparoscopic surgery is a form of MIS where surgeons operate exclusively through a single entry. However, the view from the rigid endoscope is often obscured by the instruments which pass through the same single entry. To remove the need for a secondary viewing port and the blind spots during operation, we propose a deployable wrist mechanism for minimally invasive laparoscopic surgery. It utilizes an S-shape nitinol tube with a curvature of 15 mm and 1.83 mm in diameter. When retracted, the s-shaped wrist is straightened into the main shaft of the laparoscopic tool. As the wrist translates outward, the S-shaped nitinol wrist emerges from an opening on the tool shaft and bends to point at the tooltip. The wrist has two degrees of freedom: translational displacement for controlling the bending and rotational movement of the wrist. The bending mechanism was analyzed by finite element method simulation and validated by experiments. For future work, we will try to widen the scope of its applications including laser ablation tools, triangularization, and other microsurgical procedures.**

***Index Terms*— Surgical Robotics: Laparoscopy, Minimally Invasive Surgery, Medical Robots and Systems, Soft Robot Materials, and Design.**

I. Introduction

During the last two decades, minimally invasive surgery (MIS) has become popular because it offers advantages such as less pain, faster recovery, improved cosmesis, and reduced complications [1]–[3]. Continuous efforts have been made to reduce morbidity and improve the cosmesis of MIS. These efforts include a special focus on miniaturization of equipment, the evolution of robotic surgical units, and a reduction of port size and number [4], [5].

To minimize the invasiveness, it is ideal to reduce the number and the diameter of the ports. Single-port laparoscopic/intrathoracic surgery is a rapidly evolving MIS procedure in which surgeons operate exclusively through a single entry. Single-port laparoscopic surgery (SLS) uses a single incision from 12 mm to 30 mm in size while current laparoscopic procedures use 3 to 5 trocar access ports which are 5 mm to 15 mm in diameter [6], [7]. Many clinical cases have reported that SLS lowers morbidity associated with peripheral ports with the added benefit of a single small scar versus multiple scars in conventional multi-port laparoscopic surgery [7].

Some research groups have studied expandable mechanisms [8]–[11] for creating triangulation or offering highly articulated motion in the abdominal cavity. Due to the confined space and the complexity of single-entry access, SLS is associated with a more obstructed field of view. The obscured view causes a challenge for surgeons as certain laparoscopic tools such as staplers and scissors are can cause irreversible damage. It is very challenging to develop a small endoscope (<3mm) while possessing an adjustable viewing angle. Deployable endoscopic wrist 2.5 mm or less in diameter has not been researched.

The biggest challenge in developing a wrist mechanism for the needlescopic instrument is the development of a scalable mechanism. The mechanism has to be scalable in terms of manufacturing, assembly, and control. Due to its long and slim structure, their actuators are located at the proximal end and the actuation must be transmitted along their shaft to an end-effector at the distal end. Most of the instruments use tendon-pulley mechanisms for transmission [12]–[15]. In addition, researchers used magnetic controls [16], fluidic actuators [17]–[19], smart materials [20], [21], etc. However, due to routing and tensioning, assembling tendons becomes more difficult with an increasing number of actuators and decreasing tool diameter. The length of its moment arm becomes too short to provide enough moment. Complicated structures with many actuators are costly and assembly is challenging.

In this paper, the goal of the research is to develop a scalable and deployable bending wrist to provide a view of the tooltip in laparoscopic procedures. The proposed mechanism utilizes an S-curved nitinol (Ni-Ti) with two degrees of freedom (DOF). The nitinol tube is laser patterned anisotropically to generate a high-curvature shape [22]–[24] that helps to maintain a small workspace. When stored, the mechanism is retracted in the shaft of the laparoscopic tool

This work was supported by Endopodium Inc., San Diego, CA, United States of America.

[1]Jongwoo Kim, Thomas Looi, and James Drake are with Center for Image-Guided Innovation & Therapeutic Intervention (CIGITI), The Hospital for Sick Children, University of Toronto, Toronto, ON, M5G 1X8, Canada (e-mail: kimjongwoo1988@gmail.com, thomas.looi@sickkids.ca, james.drake@sickkids.ca).

[2]Allen Newman is with Endopodium Inc., San Diego, CA, United States of America (e-mail: allen.newman@endopodium.com).

due to the super-elasticity of nitinol. When deployed, the mechanism pops up sideways which exposes a camera pointing at the tooltip. When it advances further, the wrist starts to bend according to the configuration respect to the main tool shaft. The bending can be controlled by the wrist's translational displacement. The mechanism is also able to retract back again into the tool shaft.

The contributions of this paper include the design of the deployable wrist mechanism, FEM simulation analysis, the fabrication method for the high curved s-shape tube, the workspace analysis, and the phantom SLS test. We also validated the actuation test, the workspace verification with the electromagnetic tracking, and the demonstration of the mechanism in the phantom test.

II. Design of the Instrument

Three main considerations in the design of an endoscopic wrist mechanism: 1) The deployable mechanism can pass through the trocar, 2) the mechanism needs 2 degrees of freedom (extension and rotation), and 3) the mechanism is 2.5 mm or less in diameter, both in terms of manufacturing and assembling.

A. 2-DOF Deployable Arm Mechanism

To simplify the design, the 2-DOF movement can be achieved by using an S-curved nitinol arm. This allows the arm to adjust the FOV, leading to a simple and scalable structure. The arm has translational and rotational movement along the x-axis like Fig. 1. The camera is located at the distal tip of the arm. The arm's rotational movement rotates the direction of the camera about the x-axis and the translational movement changes the x-coordinate of the camera. Once the arm advances further and has reached the edge of the main shaft's hole pattern, the wrist naturally bends upwards from the main tool shaft. The translational advancement along the +x-axis allows the arm to function as a bending wrist. The degree of translational advancement determines the bending degree of the continuum arm according to the arm's bending stiffness, EI_{arm}, where E and I_{arm} are elastic modulus and the moment of inertia of the deployable arm, respectively. The pitch angle of the camera's direction is the function of the translational displacement, δ_x, and EI_{arm}.

$$\text{pitch angle} = f(\delta_x, EI_{arm}) \quad (1)$$

The roll angle of the camera's direction is determined by the arm's rotational angle about the x-axis, ω. The upper and lower constraints of the rotational angle are determined by the width of the hole pattern of the main shaft, L_w. Considering its geometry, the boundary relation is given as (3) where r_{arm}, r_{main} are the radius of the arm and the main shaft, respectively.

$$\text{roll angle} = g(\omega) \quad (2)$$

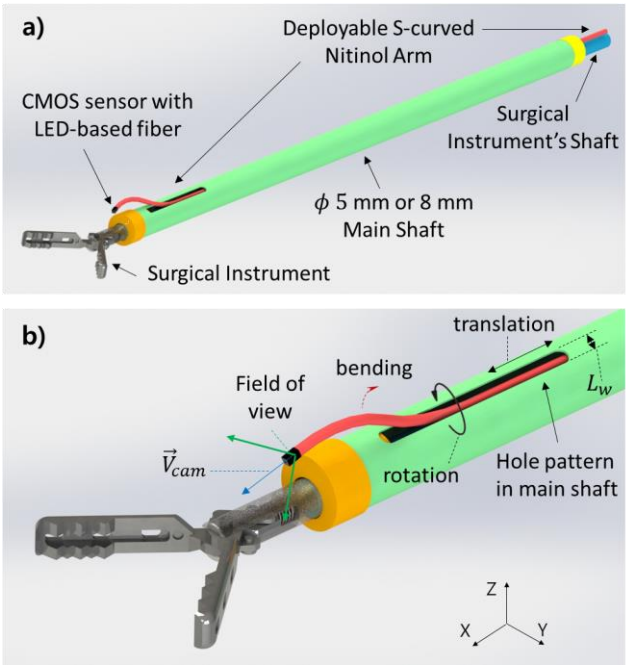

Fig. 1. a) The structure of the presented deployable mechanism for tooltip camera, b) 2-DOF movement of the deployable arm and the direction of camera.

$$-\sin^{-1}\left(\frac{L_w}{2}\right) + \tan^{-1}\left(\frac{r_{arm}}{r_{main}}\right) \le \omega \le \sin^{-1}\left(\frac{L_w}{2}\right) - \tan^{-1}\left(\frac{r_{arm}}{r_{main}}\right) \quad (3)$$

Fig. 2 indicates the design parameters of the s-shape wrist mechanism. The design parameters are set as $(r_1, r_2, \alpha, \beta) = (15\text{ mm}, 25\text{ mm}, 30°, 40°)$ so that it has a small radius of the motion envelope of 6.28 mm. $\vec{V}_{cam}$ is the unit vector to represent the camera's direction. $\vec{V}_{cam,i}$ is $\vec{V}_{cam}$ at the initial point and $\vec{V}_{cam,i}$ directs $-10.58°$ with respect to the +x-axis.

To retract the wrist, a negative translational movement is applied and the NiTi wrist is straightened as it is pulled within the main tool shaft. When popped out again, the arm restores its s-shape structure.

The FOV is controlled by combining the rotation and translation movements of the deployable arm. The camera's direction can be represented by rotation about z-axis by ω and the rotation about y-axis by $f(\delta_x, EI_{arm})$ as (4) and (5). It is difficult to formulate an analytical solution of (1) since it is a continuum bending wrist with micropatterning. The relationship of (1) is studied in section III, and then the camera direction can be controlled by (5).

$$\vec{V}_{cam} = \vec{V}_{cam,i}\ \text{Rot}(z, \omega)\ \text{Rot}(y, f(\delta_x, EI_{arm})) \quad (4)$$

$$\vec{V}_{cam} = \begin{bmatrix} \cos 10.58° \\ 0 \\ -\sin 10.58° \end{bmatrix} \begin{bmatrix} \cos\omega & -\sin\omega & 0 \\ \sin\omega & \cos\omega & 0 \\ 0 & 0 & 1 \end{bmatrix} \text{Rot}(y, f(\delta_x, EI_{arm})) \quad (5)$$

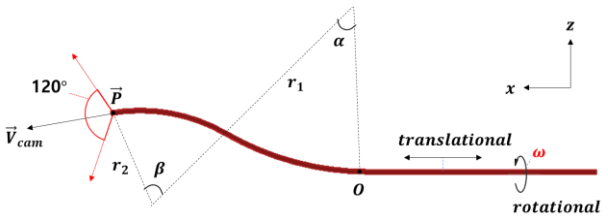

Fig. 2. a) The design of the deployable wrist. When $(r_1, r_2, \alpha, \beta) = (15\text{mm}, 25\text{mm}, 30°, 40°)$, the radius of the motion envelope is only 6.28mm. The camera sensor has its own 120 degrees of FOV.

B. *Manufacturing of the Deployable Bending Wrist*

The wrist was pre-shaped in the s-curved design. As presented in Fig. 2, the proximal section is an arc with a central angle of 40 degrees and a radius of curvature of 15 mm; the second section is an arc with a central angle of 30 degrees and a radius of curvature of 25 mm. the proximal section is a 40-degree curve with a radius of curvature of 15 mm and the second part made a 30-degree curve with 25 mm. The wrist is made of a nitinol tube with 1.83 mm of the outer diameter and 1.54 mm of the inner diameter. To achieve a minimum radius of curvature is 15 mm, a specialized manufacturing process is required. It is as follows: 1) the nitinol tube was asymmetrically laser patterned to have higher curvature, and 2) the deployable arm was shape-set through the two-step heat treatment [23].

The asymmetric patterns illustrated in Fig. 3a reduces the bending stiffness along the bending direction, so it enables the higher curvature of the tube. At the same time, the asymmetric pattern maintains torsional rigidity and the flexural rigidity along the non-patterned area of Fig. 3a compared to the universal patterning [22], [24], [25]. Thus, the asymmetrically patterned deployable arm is more stable as it has a higher threshold for buckling, as opposed to the universal patterns.

The through-hole patterns on the nitinol tube were created by laser cutting (RT1000 Laser Tube Cutting Machine, Preco Inc., KS, USA), where feed rate is 127 mm/min, the duty cycle is 12%, power is 250 watts, and pulse frequency is 500Hz, as shown in Fig. 3b.

For the shape setting, an aluminum jig was manufactured as seen in Fig. 3c. Since the high curvature cannot be shaped by a single heat treatment process, the heat treatment process was performed twice: the first used a low curvature jig and the second used a high curvature jig. After the two heat treatment steps, the deployable arm was shaped into the

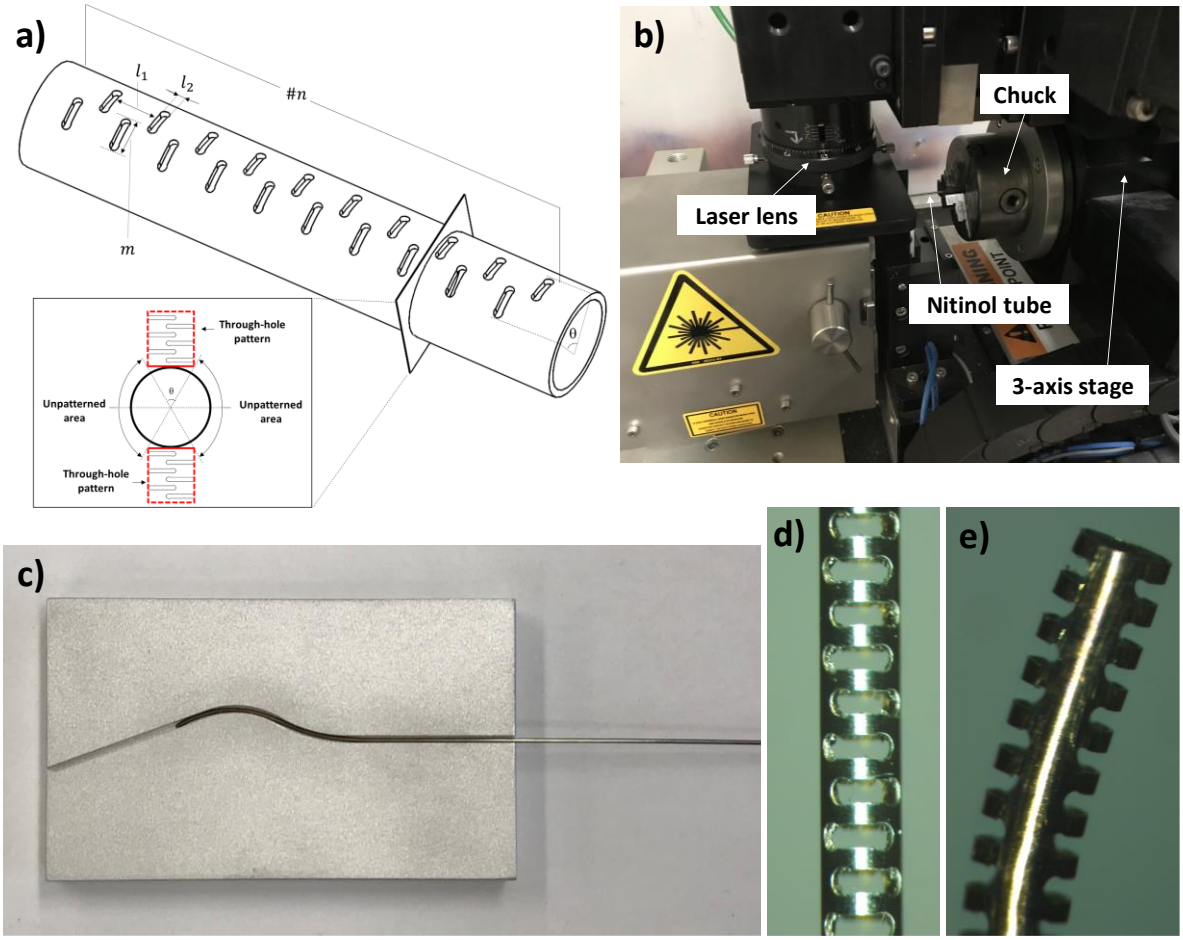

Fig. 3. a) The diagram and the design parameters of non-uniform through-hole pattern on the nitinol tube. A pair of columns were engraved and each column has $\theta = 134°$ of the central angle. b) the automized laser machining set-up with RT1000 Laser Tube Cutting Machine, Preco Inc., USA. c) the jig of the bending wrist for the heat treatment. d) the microscopic photograph of the laser-machined nitinol tube. e) the microscopic photograph of the tube's distal part after heat treatment.

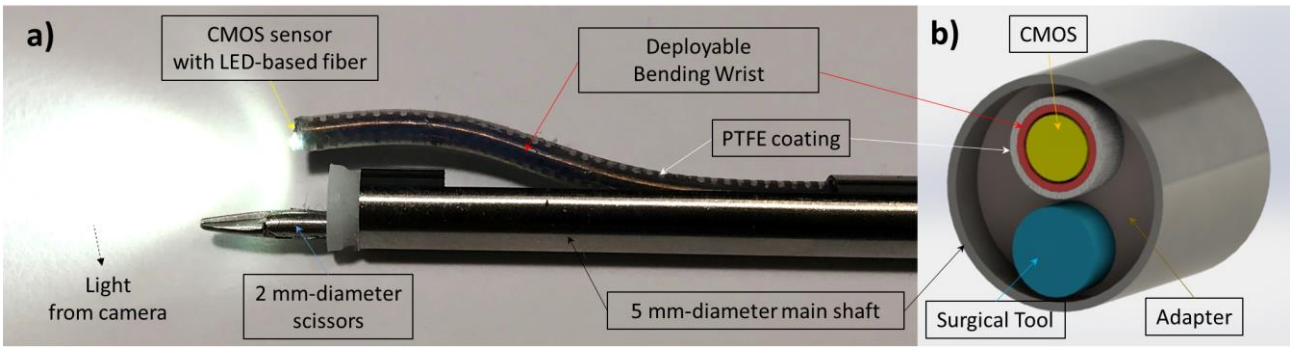

Fig. 4. a) The assembled structure. The deployable wrist is PTFE coated and equipped with the camera at the distal tip. The light emits from the distal tip of the wrist and the camera wires pass through the hollow space of the wrist. b) the cross-section view of the assembled structure. It demonstrates how surgical instrument, camera, wires, and the wrist are integrated into 5 mm-diameter main shaft.

designated design. For each heat treatment, the patterned tube was placed in the jig, annealed in the furnace (3-1750, Vulcan Muffle Furnace, Neytech, USA) for 28 minutes at 530°C, and then quenched in room temperature water.

Through laser machining and a two-step heat treatment, the deployable arm was shape-set to the desired curvature. The arm was integrated into the main shaft, and a laparoscopic tool (such as grasping forceps or scissors) was inserted into the working channel, as shown in Fig. 4. The proposed mechanism is well compatible with existing tools of 2 mm, 5 mm, and others in diameter. The detailed assembly is demonstrated in Fig. 4b.

C. Assembling the Deployable Bending Wrist

The main shaft contains the deployable patterned tube with a coating and surgical instrument. Fig. 4 demonstrates the assembly when a 2 mm-diameter end effector is utilized. The centers of the camera and end effector lie on the vertical line that passes the center of the main shaft. The bending wrist's center is located 0.95 mm higher in the z-axis from the center of the main shaft.

The endoscopic camera (minnieScope -XS ENA-10005-AS, EC3-L04-F5-T1, Enable, Inc., CA, USA) passes through the hollow space of the deployable arm and is connected to the power source, and its CMOS sensor is located at the distal tip of the arm. The camera has 120 degrees of FOV lens with depth of field 2.5 mm – 70 mm. LED-based fiber offers light for image sensing. The light source is shown in Fig. 4. Ultrahigh NA fiber (NA>0.82) is used to match the high FOV of the lens. The CMOS sensor has 1M pixel resolution and 1.40 mm of the outer diameter and its electric cable thickness is 1.20 mm.

Polytetrafluoroethylene (PTFE) heat shrink tube (2:1 shrink ratio, AWG 17, Zeus, USA) was used to coat the patterned bending wrist. The coating lowers friction between shafts and conceals the through-hole patterns of the wrist.

The wrist can be integrated into commercial surgical instruments. According to the diameter of the instrument, a 5 mm or 8 mm-diameter main shaft was employed to assemble the surgical instrument and deployable endoscope arm.

III. FEM Simulation & Experiments

A. Finite Element Methods (FEM) Simulation

AFEM simulation was developed to study the behavior of the tool. Using the FEM, we are able to predict the deformation of the deployable arm as it advances along the positive x-axis. In the FEM model, we constrained the rotation about z and x-axes and the deformation along the y-axis. We used two distinguished methods for the simulation through ANSYS 2019, USA. In the first method, we replaced the patterned part with the non-patterned tube structure of effective bending stiffness value, as illustrated in Fig. 5a (Simulation A). The calculation of the effective bending stiffness was based on our previous study [22], [24]. In the second method, we used the patterned tube model for analysis, as illustrated in Fig. 5b (Simulation B). The grey figures represent the undeformed structure at the beginning. The simulation results are compared to the experimental results in the following section.

B. Electromagnetic Tracking Test on the Deployable Wrist

We set up a motorized control system to examine 2-DOF motion control of deployable wrist by 1) controlling the FOV, and 2) retracting/extending the arm. As shown in Fig. 6, the wrist is held by the collet chuck and the motorized stage

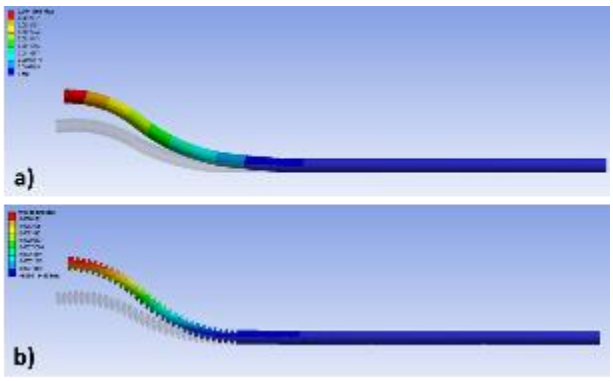

Fig. 5. The FEM simulation results using a) effective bending stiffness model, b) patterned tube structure

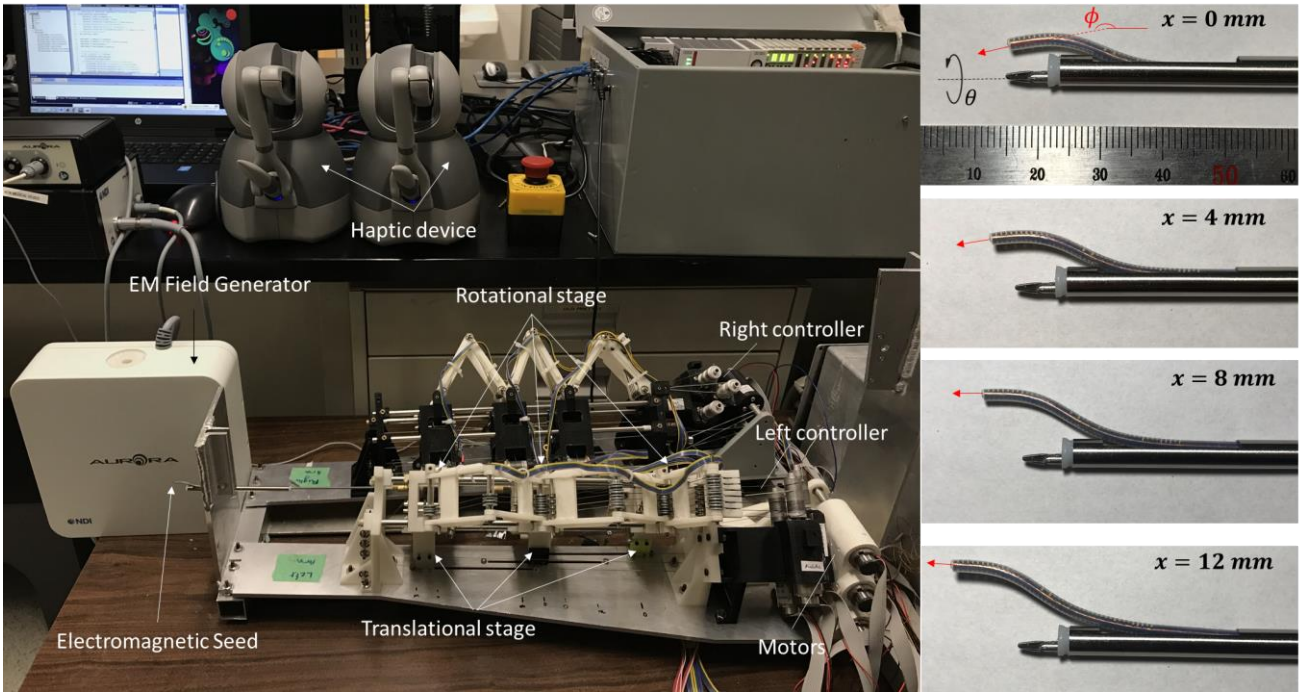

Fig. 6. The set ups for electromagnetic tracking. The right column demonstrates the photographs of the selected configuration of the mechanism when x=0, 4, 8, 12 mm, respectively. When x=0, the deployable arm starts in contact with the proximal edge of the main shaft's hole pattern. The upper right figure indicates θ and ϕ angles to represent the direction. The red arrow represents the direction of the camera.

controls the rotational and translational movement of the wrist. The user can control the direction of the end tip by stylus haptic device (Geomagic touch, 3D systems, USA) or command joint values of each translational and rotational stage. The electromagnetic tracking experiment was performed to examine the direction of the distal tip. A 5-DOF electromagnetic needle sensor was equipped at the distal tip of the deployable arm. The electromagnetic tracking system (Aurora, Northern Digital, Waterloo, ON, Canada) was installed to track the sensor as shown in Fig. 6. The direction of the sensor was synchronized with the direction of the distal tip. The direction and the position of the distal tip are determined by the rotational and translational movement of the arm.

To characterize the workspace, we translated the wrist from 0 to 12 mm and rotated the wrist from 41.1 to 138.9 deg. (see Fig. 6). The discrete data points were $x \in \{0, 2\ mm, 4\ mm, 6\ mm, 8\ mm, 10\ mm, 12\ mm\}$ and the roll angle, $\theta \in \{45°, 60°, 75°, 90°, 105°, 120°, 135°\}$, summing up 49 cases. The direction measurement was repeated five times and the average value was taken for each case. The standard deviation is 2.37 ° for the 49 cases. Table I demonstrates the results of the direction of the distal tip in terms of (θ, ϕ). θ and ϕ are roll and pitch, respectively, as illustrated in Fig. 6. The experimental results when $\theta = 90°$ are compared with the simulation data in Table II. The effective bending stiffness model showed more consistency with the experimental results. The red number in Table II indicates the error of the simulation results compared to experimental results. The average errors for simulation A and B are 4.87 and 7.67 degrees, respectively. The degree of the error increases as the tube advances further (x value increases). Fig. 7 illustrates the field of view (FOV) diagram of the proposed wrist with the equipped camera that has 120 degrees FOV. The diagram assumes the main shaft is fixed and only considers the movement of the wrist. The expanded FOV was tested in the phantom test of the following section.

To analyze the fatigue, the wrist was extended and retracted

TABLE I. THE DIRECTION (θ, Φ) OF THE DISTAL TIP MEASURED BY EM TRACKER

	45°	**60°**	**75°**	**90°**	**105°**	**120°**	**135°**
0 mm	45.1°, 190.6°	59.7°, 189.3°	75.5°, 188.9°	91.2°, 192.5°	106.1°, 190.0°	120.5°, 189.4°	134.3°, 189.2°
2 mm	46.0°, 186.6°	61.2°, 184.7°	73.7°, 184.6°	89.6°, 184.5°	106.0°, 188.3°	119.6°, 185.3°	136.4°, 188.8°
4 mm	44.3°, 185.9°	58.6°, 186.1°	74.2°, 184.0°	90.5°, 182.9°	103.9°, 184.6°	118.7°, 184.0°	133.7°, 182.8°
6 mm	45.5°, 180.2°	59.7°, 183.2°	75.7°, 183.8°	91.0°, 183.0°	104.1°, 181.9°	120.7°, 181.3°	136.2°, 180.6°
8 mm	45.4°, 180.5°	58.7°, 178.0°	74.7°, 179.3°	89.4°, 179.9°	104.9°, 178.0°	120.4°, 178.0°	134.7°, 176.6°
10 mm	44.2°, 178.5°	59.6°, 177.8°	75.3°, 175.2°	88.9°, 178.9°	104.2°, 178.7°	118.9°, 175.0°	134.3°, 177.5°
12 mm	45.3°, 175.2°	60.1°, 173.9°	73.8°, 172.1°	91.0°, 173.6°	104.2°, 173.5°	120.8°, 173.5°	135.0°, 174.7°

TABLE II. THE COMPARISON BETWEEN EXPERIMENT AND SIMULATION RESULTS ON THE PITCH DIRECTION OF THE END TIP

	0 mm	2 mm	4 mm	8 mm	10 mm	12 mm
Simulation A	190.2° (2.3)	182.2° (2.3)	179.5° (3.4)	178.5° (4.5)	172.3° (7.6)	164.5° (9.1)
Simulation B	190.2° (2.3)	179.2° (5.3)	176.7° (6.2)	174.2° (8.8)	169.9° (10.0)	160.2° (13.4)
Experiment	192.5°	184.5°	182.9°	183.0°	179.9°	173.6°

from 0 to 12mm for 450 cycles. After the testing, the wrist remained functional and did not exhibit failure.

C. The Phantom test of Laparoscopic Surgery

The goal of this test is to examine the nearby environments and monitor the surroundings of the end effector for safe and minimally invasive operations. In the experiment, we integrated the 5mm-diameter graspers (Endopath, Ethicon endo-surgery, USA) to our proposed wrist and tested is on the laparoscopic training system (T3 series, 3D-Med, OH, USA). Inside the training system, we put uneven terrain in the training box and then attempted to grasp the target tissue with proper visual feedback through a single port. During the test, we used the deployable endoscopic wrist to adjust the view angle when it was obstructed. The endoscope at the wrist's distal tip offers a detailed view of the end-effector and its surroundings. The 1Mpixel high resolution of camera view lets users distinguish nearby tissues clearly. Three surgeons validated that the mechanism offered proper endoscopic visual feedbacks. In SLS, the area under the tooltip may not be visible, but the proposed mechanism can monitor the underneath area and safely identify the target tissue. The supplementary video visually demonstrates how the proposed deployable wrist contributes to the single-port laparoscopic surgery. Further clinical tests will proceed in future work.

IV. DISCUSSION

The proposed bending wrist offers a deployable and scalable mechanism with a 2-DOF capability to adjust the viewing angle. The proposed bending wrist is scalable and can be straightened to pass through a small diameter trocar. In this paper, its diameter is only 1.83 mm without coating or 2.15 mm with PTFE coating.

The proposed wrist does not need axillary actuators or bulky structures. The wrist's rotational and translational movements can be controlled at the proximal side by motors or manually. The simple and scalable design ease the difficulties of assembling in a smaller dimension.

In addition, surgeons emphasized that monitoring the 360° view with respect to the end effector helps them to recognize the target tissue exactly during surgical manipulation. The proposed wrist is deployed adjacent to the main shaft. The wrist is translated, rotated, and bent to change the field of view (FOV) to reduce the unreachable area with rigid endoscopes. In the experiment, the wrist offers 97.8 degrees of independent roll motion and 18.9 degrees of pitch motion.

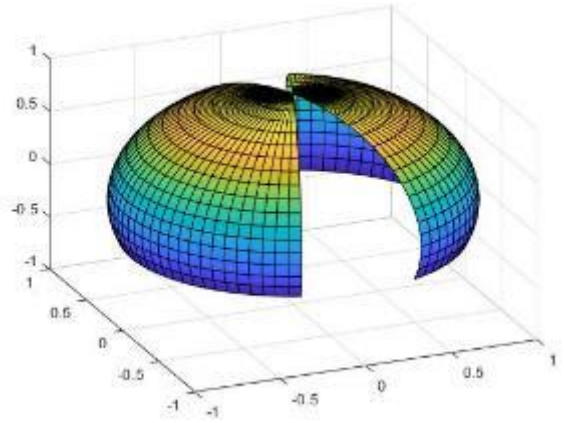

Fig. 7. The field of view (FOV) diagram of the proposed wrist, considering the equipped camera with 120 degrees FOV. The diagram assumes the main shaft fixed. Note that the direction is expressed as a unit vector.

It is expected to contribute to reducing the unreachable area in SLS or the need for multiple ports to minimize invasiveness.

All materials are biocompatible and sterilizable: the main shaft is made of stainless steel, the deployable arm of nitinol, and the PDMS coatings. The connecting parts can be replaced by stainless steel or titanium. The PTFE (Polytetrafluoroethylene) coating is applied to lower friction between the deployable arm and the main shaft. The coating also offers the sealing for the through-hole patterns of the deployable arm.

In the simulation, we validated the tendency of the bending wrist movement. The model with the effective bending stiffness demonstrated better fitting with the experimental results. However, we still needed to compensate for the large deformation cases of the bending wrist motion. There are potential errors and limits in the data. In the experiments, we saw that the electromagnetic sensor can be influenced by nearby metals and magnets. The tolerance between shafts can slightly affect the results. We need to consider these error sources.

In terms of cost, the nitinol is expensive material in this mechanism. Alternatively, the deployable arm can consist of the curved nitinol part and the straight stainless steel part to save the cost. The two parts can be connected by laser welding [26]. Discussed in section II, the bending wrist can be integrated into commercial surgical instruments. We tested the assembly with the laparoscopic graspers and scissors with 5 mm and 1.9 mm in diameter. In addition, the wrist can be used for laser ablation.

Due to a lack of scalable and highly articulated wrists, triangularization has been difficult to achieve in SLS systems [27]. Its pre-curved shape has the high curvature and the curvature is adjusted through bending. As illustrated in Fig. 6, we plan to employ the two s-curved wrists for both left and right controllers. The wrists keep straight when they are restored at the main shaft. When advanced and deployed, they can form triangularization using their s-curved structure. In

addition, the 6-DOF controller will be utilized to integrate with other tubular mechanisms.

In future work, we will try to widen the scope of the applications of the wrist mechanism using three-dimensional (3D) curved shape. The current design of the deployable arm is based on an s-curved shape in 2D. Three-dimensionally curved design allows flexibility in customizing workspace and the sweeping volume of the deployable arm. Thanks to its simple mechanism and scalability, the wrist will apply to microsurgical applications.

REFERENCES

[1] F. Bagante *et al.*, "Minimally Invasive vs. Open Hepatectomy: a Comparative Analysis of the National Surgical Quality Improvement Program Database," *J. Gastrointest. Surg.*, vol. 20, no. 9, pp. 1608–1617, 2016.

[2] G. Gandaglia *et al.*, "Effect of minimally invasive surgery on the risk for surgical site infections results from the national surgical quality improvement program (nsqip) database," *JAMA Surg.*, vol. 149, no. 10, pp. 1039–1044, Oct. 2014.

[3] C. Tsui, R. Klein, and M. Garabrant, "Minimally invasive surgery: National trends in adoption and future directions for hospital strategy," *Surg. Endosc.*, vol. 27, no. 7, pp. 2253–2257, Jul. 2013.

[4] V. Vitiello, S. L. Lee, T. P. Cundy, and G. Z. Yang, "Emerging robotic platforms for minimally invasive surgery," *IEEE Rev. Biomed. Eng.*, vol. 6, pp. 111–126, 2013.

[5] J. Burgner-Kahrs, D. C. Rucker, and H. Choset, "Continuum Robots for Medical Applications: A Survey," *IEEE Trans. Robot.*, vol. 31, no. 6, pp. 1261–1280, Dec. 2015.

[6] J. R. Romanelli and D. B. Earle, "Single-port laparoscopic surgery: An overview," *Surg. Endosc.*, vol. 23, no. 7, pp. 1419–1427, 2009.

[7] I. Ahmed and P. Paraskeva, "A clinical review of single-incision laparoscopic surgery," *Surgeon*, vol. 9, no. 6, pp. 341–351, 2011.

[8] S. Il Kwon *et al.*, "Design and fabrication of transformable head structures for endoscopic catheters∗," in *Proceedings - IEEE International Conference on Robotics and Automation*, May 2019, vol. 2019-May, pp. 373–378.

[9] E. A. Arkenbout, P. W. J. Henselmans, F. Jelínek, and P. Breedveld, "A state of the art review and categorization of multi-branched instruments for NOTES and SILS," *Surg. Endosc.*, vol. 29, no. 6, pp. 1281–1296, Jun. 2015.

[10] K. Xu, R. E. Goldman, J. Ding, P. K. Allen, D. L. Fowler, and N. Simaan, "System design of an insertable robotic effector platform for Single Port Access (SPA) surgery," in *2009 IEEE/RSJ International Conference on Intelligent Robots and Systems, IROS 2009*, Oct. 2009, pp. 5546–5552.

[11] K. Xu, J. Zhao, and M. Fu, "Development of the SJTU Unfoldable Robotic System (SURS) for Single Port Laparoscopy," *IEEE/ASME Trans. Mechatronics*, vol. 20, no. 5, pp. 2133–2145, Oct. 2015.

[12] S. M. Segreti, M. D. M. Kutzer, R. J. Murphy, and M. Armand, "Cable length estimation for a compliant surgical manipulator," in *Proceedings - IEEE International Conference on Robotics and Automation*, May 2012, pp. 701–708.

[13] P. Breedveld, H. G. Stassen, D. W. Meijer, and J. J. Jakimowicz, "Manipulation in laparoscopic surgery: Overview of impeding effects and supporting aids," *J. Laparoendosc. Adv. Surg. Tech. - Part A*, vol. 9, no. 6, pp. 469–480, Dec. 1999.

[14] D. C. Rucker, R. J. Webster, G. S. Chirikjian, and N. J. Cowan, "Equilibrium conformations of concentric-tube continuum robots," *Int. J. Rob. Res.*, vol. 29, no. 10, pp. 1263–1280, Sep. 2010.

[15] D. J. Podolsky *et al.*, "Utilization of Cable Guide Channels for Compact Articulation Within a Dexterous Three Degrees-of-Freedom Surgical Wrist Design," *J. Med. Devices, Trans. ASME*, vol. 13, no. 1, Mar. 2019.

[16] M. Simi, R. Pickens, A. Menciassi, S. D. Herrell, and P. Valdastri, "Fine tilt tuning of a laparoscopic camera by local magnetic actuation: Two-port nephrectomy experience on human cadavers," *Surg. Innov.*, vol. 20, no. 4, pp. 385–394, Aug. 2013.

[17] A. De Greef, P. Lambert, and A. Delchambre, "Towards flexible medical instruments: Review of flexible fluidic actuators," *Precis. Eng.*, vol. 33, no. 4, pp. 311–321, Oct. 2009.

[18] M. Cianchetti, T. Ranzani, G. Gerboni, I. De Falco, C. Laschi, and A. Menciassi, "STIFF-FLOP surgical manipulator: Mechanical design and experimental characterization of the single module," in *IEEE International Conference on Intelligent Robots and Systems*, Nov. 2013, pp. 3576–3581.

[19] G. Gerboni, T. Ranzani, A. Diodato, G. Ciuti, M. Cianchetti, and A. Menciassi, "Modular soft mechatronic manipulator for minimally invasive surgery (MIS): overall architecture and development of a fully integrated soft module," *Meccanica*, vol. 50, no. 11, pp. 2865–2878, Nov. 2015.

[20] V. De Sars, S. Haliyo, and J. Szewczyk, "A practical approach to the design and control of active endoscopes," *Mechatronics*, vol. 20, no. 2, pp. 251–264, Mar. 2010.

[21] K. Ikuta, M. Tsukamoto, and S. Hirose, "Shape Memory Alloy Servo Actuator System With Electric Resistance Feedback and Application for Active Endoscope.," Apr. 1988, pp. 427–430.

[22] D. Y. Lee *et al.*, "Anisotropic Patterning to Reduce Instability of Concentric-Tube Robots," *IEEE Trans. Robot.*, vol. 31, no. 6, pp. 1311–1323, 2015.

[23] J. Kim, W. Lee, S. Kang, K. J. Cho, and C. Kim, "A Needlescopic Wrist Mechanism with Articulated Motion and Kinematic Tractability for Micro Laparoscopic Surgery," *IEEE/ASME Trans. Mechatronics*, vol. 25, no. 1, pp. 229–238, 2020.

[24] J. Kim, W. Y. Choi, S. Kang, C. Kim, and K. J. Cho, "Continuously Variable Stiffness Mechanism Using Nonuniform Patterns on Coaxial Tubes for Continuum Microsurgical Robot," *IEEE Trans. Robot.*, vol. 35, no. 6, pp. 1475–1487, 2019.

[25] K. A. Xin Jue Luo, T. Looi, S. Sabetian, and J. Drake, "Designing Concentric Tube Manipulators for Stability Using Topology Optimization," *IEEE Int. Conf. Intell. Robot. Syst.*, pp. 1764–1769, 2018.

[26] P. C. Hall, "Nitinol joined to stainless steel by laser welding," in *Advanced Materials and Processes*, 2004, vol. 162, no. 2, p. 18.

[27] R. J. Nelson, J. S. S. Chavali, N. Yerram, P. Babbar, and J. H. Kaouk, "Current status of robotic single-port surgery," *Urology Annals*, vol. 9, no. 3. Medknow Publications, pp. 217–222, Jul. 01, 2017.